ADVANCED FUNCTIONAL MATERIALS
www.afm-journal.de

Edge-Fluorinated Graphene Nanoplatelets as High Performance Electrodes for Dye-Sensitized Solar Cells and Lithium Ion Batteries

In-Yup Jeon, Myung Jong Ju, Jiantie Xu, Hyun-Jung Choi, Jeong-Min Seo, Min-Jung Kim, In Taek Choi, Hong Mo Kim, Jae Cheon Kim, Jae-Joon Lee, Hua Kun Liu, Hwan Kyu Kim, Shixue Dou,* Liming Dai,* and Jong-Beom Baek**

Edge-selectively fluorinated graphene nanoplatelets (FGnPs) are prepared by mechanochemically driven reaction between fluorine gas (20 vol% in argon) and activated carbon species from graphitic C–C bonds unzipped by high-speed stainless steel balls with a high kinetic energy. The fluorination at edges of the unzipped graphene nanoplatelets (GnPs) is confirmed by various analytical techniques while the content of fluorine in FGnPs is determined to be 3.0 and 3.4 at% by X-ray photoelectron spectroscopy and energy-dispersive X-ray spectroscopy, respectively. Because of the large difference in electronegativity between carbon ($\chi = 2.55$) and fluorine ($\chi = 3.98$) and the strong C–F bond, the edge-fluorination of GnPs can provide the maximized charge polarization with an enhanced chemical stability. Thus, electrodes based on the resultant FGnPs demonstrate superb electrochemical performance with excellent stability/cycle life in dye-sensitized solar cells (FF: 71.5%; J_{sc}: 14.44 mA cm^{-2}; V_{oc}: 970 mV; PCE: 10.01%) and lithium ion batteries (650.3 mA h g^{-1} at 0.5 C, charge retention of 76.6% after 500 cycles).

1. Introduction

The continuously increasing global energy consumption has led to a surge in energy production from renewable natural sources, such as solar, wind, hydro, and geothermal heat.[1] However, these natural energy sources are sporadic and localized, which need to be efficiently stored and delivered on demand to meet requirements for specific applications, such as mobile electronic devices. Although a variety of energy conversion and storage devices, such as solar cells, fuel cells, hydrogen storages, lithium ion batteries (LIBs), and supercapacitors,[2] have been developed, their commercial applications will not be fully realized if there is no large-scale capability for the low-cost development of stable materials with high performance for energy conversion and storage.

Carbon materials, such as fullerenes, carbon nanotubes, nanodiamonds, graphene, graphite, and amorphous carbon, have been playing a significant role in the development of alternative clean and sustainable energy sources due to their unique and technically important properties. Specifically, graphene, a one-atom-thick graphitic layer comprising sp^2 hybridized carbon atoms,[3] has demonstrated many peculiar properties, including superior electrical conductivity,[4] large surface area (≈2630 m^2 g^{-1}),[5] excellent mechanical property,[6] and high thermal/chemical stability.[7] These unusual properties make graphene as one of the promising electrocatalysts and electrode materials for electrochemical energy conversion and storage. In this regard, the oxidative corrosion (e.g., $C + O_2 \rightarrow CO_2$) of carbon-based electrodes is one of the most critical drawbacks leading to a short lifetime of energy conversion and storage devices.[8,9] The typical half lifetime (50% charge capacity retension) of mobile phone battary is less than one year, and also the common pitfall for the commerciallization of electric vehicle is short battary lifetime. Therefore, it is important to develop carbon-based electrode materials with strong chemical bonds and enhanced charge polarization to reduce the overpotentials for energy-related electrochemical reactions,[10] and hence less susceptible to the oxidative corrosion (e.g., $C + O_2 \rightarrow CO_2$). Fluorine ($\chi = 3.98$) is the most electronegative element among

Dr. I.-Y. Jeon, H.-J. Choi, J.-M. Seo, M.-J. Kim, Prof. J.-B. Baek
School of Energy Engineering/Low-Dimensional Carbon Materials Center
Ulsan National Institute of Science and Technology (UNIST)
UNIST-gil 50, Ulsan 689-798, Korea
E-mail: jbbaek@unist.ac.kr
Dr. M. J. Ju, I. T. Choi, H. M. Kim, Prof. H. K. Kim
Global GET-Future Lab. and Department of Advanced Materials Chemistry
Korea University, Sejong 339-700, Korea
E-mail: hkk777@korea.ac.kr
Dr. J. Xu, H. K. Liu, Prof. S. Dou
Institute for Superconducting and Electronic Materials
University of Wollongong
Wollongong, NSW 2522, Australia
E-mail: dou@uow.edu.au
J. C. Kim, Prof. J.-J. Lee
Nanotechnology Research Center and Department of Applied Life Science Konkuk University
Chungju 380-701, Korea
Prof. L. Dai
Department of Macromolecular Science and Engineering
Case Western Reserve University
Cleveland, OH 44106, USA
E-mail: liming.dai@case.edu

DOI: 10.1002/adfm.201403836

elements in the periodic table and the bond strength of C–F bond (488 kJ mol^{-1}) is the strongest single covalent bond. Hence, fluorination of graphene could provide the maximum charge polarization for enhanced electrochemical activity of energy-related reactions and excellent electrode stability. However, the fluorination of carbon-based materials to form C–F bonds is very limited, because handling fluorine (F_2) gas for direct formation of C–F bonds is too dangerous for laboratory use. As an alternative approach, xenon difluoride (XeF_2) has been used for fluorination of graphene,[11] though not as a general method because XeF_2 is very toxic and too expensive. Furthermore, the XeF_2 fluorination occurs not only on the graphitic basal plane but also at its edges, scarifying the outstanding electronic and structural characteristics intrinsically associated with the graphene basal plane. Unlike the precedent approaches, we have developed a new efficient approach to edge-selectively functionalized graphene nanoplatelets (EFGnPs) with various functional groups and/or heteroatoms via the simple but efficient ball-milling-induced mechanochemical reactions.[12–14]

In this study, we have, for the first time, been able to introduce fluorine at the edges of graphene nanoplatelets (GnPs) by the ball-milling process under well-optimized conditions. Since handling fluorine requires extreme care (Caution!!! High concentration of fluorine gas cannot be handled in ordinary laboratory condition), we optimized and performed the "direct" fluorination by using diluted fluorine gas (20 vol%) in argon to safely realize edge-fluorination under the normal laboratory conditions. The resultant edge-selectively fluorinated GnPs (FGnPs) were demonstrated to display excellent electrocatalytic performance and electrode stability (or cycle life) in dye-sensitized solar cells (DSSCs) and LIBs. Therefore, the scalable and cost-effective ball-milling technology could lead to mass production of FGnPs at low cost to satisfy commercial needs for energy conversion and storage applications.

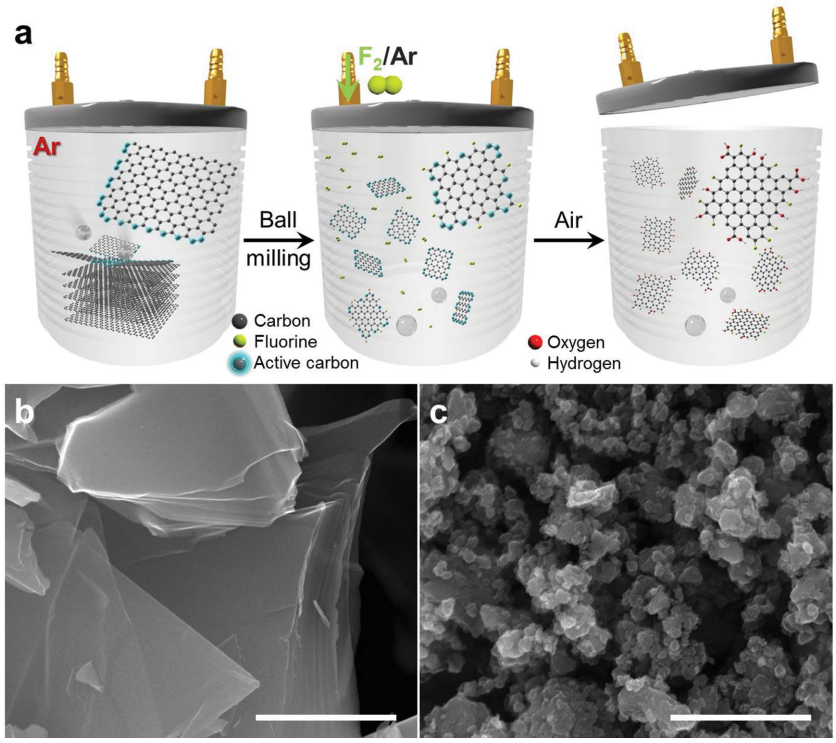

Figure 1. Preparation of edge-fluorinated graphene nanoplatelets (FGnPs) and morphological change of before and after ball-milling: a) Schematic of the mechanochemically driven reaction between active carbon species at the edges of graphene and fluorine gas (20 vol% in argon) to produce FGnPs. SEM images: b) before ball-milling, the pristine graphite with a large grain size (<150 μm); c) after ball-milling, FGnPs show a much smaller grain size (<300 nm). Scale bars are 1 μm. Compared to the pristine graphite, the dramatic grain size reduction of FGnPs implicates that the unzipping of graphitic C–C bonds generates active carbon species, which react with fluorine gas for the formation of C–F bonds at the broken edges.

2. Results and Discussion

As schematically represented in **Figure 1**a (the detailed mechanism is proposed in Figure S1, Supporting Information), the larger grain size of graphite was first mechanochemically crushed into the smaller grain size of edge-activated GnPs by ball-milling-induced unzipping the graphitic C–C bonds in graphite under argon atmosphere. Diluted fluorine gas was then slowly injected into ball-mill container, in which one of the most reactive chemical species (mostly carboradicals at the broken edges) reacted with fluorine to yield FGnPs (Experimental in the Supporting Information). Scanning electron microscopy (SEM) images show a large grain size (<150 μm, Figure 1b) and the dramatically reduced grain size (<300 nm, Figure 1c) for the pristine graphite and the resultant FGnPs, respectively. Field emission (FE)-SEM energy-dispersive X-ray spectroscopy (EDS) (Figure S2a, Supporting Information) and the corresponding element mapping (Figure S3, Supporting Information) show that FGnPs consist of carbon, oxygen, and fluorine, while the pristine graphite has mostly carbon with trace of oxygen without fluorine (Figure S3, Supporting Information). The content of fluorine in FGnPs by EDS is about 3.4 at% (Table S1, Supporting Information). Furthermore, the typical bright field (BF) and dark field (DF) images of scanning transmission electron microscopy (STEM) with corresponding EDS spectrum show the presence of fluorine together with carbon and oxygen (Figures S5a–e, Supporting Information). The EDS mappings further confirm the presence of carbon, oxygen, and fluorine in the FGnPs (Figures S5f–i, Supporting Information). The presence of oxygen is due to the termination of remnant carbon species with air/moisture (i.e., O_2, CO_2, and H_2O) into oxygen-containing functional groups (e.g., –OH, –COOH) upon opening the ball-milling reactor (Figure S1, Supporting Information). As a control experiment, pristine graphite-diluted fluorine gas was charged without stainless steel balls and agitated for 48 h, but there was no trace of fluorine detected, suggesting diluted fluorine gas was not reactive

enough for the fluorination of graphitic framework. These results indicate that the occurrence of the cracking of graphitic C–C bonds and the subsequent edge-fluorination were only induced by high speed ball-milling graphite in the presence of diluted fluorine gas. The detected fluorine must be from those C–F bonds at the edges of FGnPs as unreacted fluorine, if any, has been spontaneously evacuated from the ball-mill container by opening the lid and work-up procedures (Experimental details in the Supporting Information).

X-ray photoelectron spectroscopy (XPS) was further utilized for detecting element compositions of the samples. As expected, the pristine graphite shows a dominant C1s peak with a minor O1s band attributable to physically adsorbed oxygen onto the graphite surface (**Figure 2**a).[15] FGnPs exhibit a unique F1s peak in addition to the C1s and O1s peaks. The content of fluorine in FGnPs by XPS is about 3.0 at% (Table S1, Supporting Information), which is agreed well with the FE-SEM EDS result (3.4 at%). The high-resolution C1s peak of FGnPs could be deconvoluted into three components of C=C (284.2 eV), C–O (285.9 eV), and C=O (288.5 eV). The C=O peak is overlapped with C–F (Figure S6a, Supporting Information),[16] while the O1s peak is divided into two chemical bonds of C=O (531.9 eV) and C–O (533.3 eV) (Figure S6b, Supporting Information) arising from the termination of remnant active carbon species with air/moisture upon opening the lid for the work-up procedures (Experimental details in the Supporting Information). The F1s peak shows single sp^2 C–F component at 687.3 eV (Figure 2b), confirming that the edges of FGnPs consist of covalent C–F bonds. Furthermore, the ^{19}F magic angle spinning (MAS) nuclear magnetic resonance (NMR) spectrum of the FGnPs was acquired, which displayed a broad-band centered at −167.5 ppm over −50 to −300 ppm (Figure 2c) characteristic of the rigid fluorinated carbon lattice. This peak is attributed to sp^2 C–F bonds[17] and the line broadening is due to strong ^{19}F–^{19}F homonuclear dipolar coupling[18,19] of different C–F bonds at the FGnP edges, such as the armchair C–F and zigzag C–F (Figure S1, Supporting Information).

Thermogravimetric analysis (TGA) was used for the quantification of fluorination. Since combustion of fluorinated compounds in the presence of oxygen (air) does not give reliable data,[20] TGA measurements were conducted under nitrogen atmosphere. The char yields of the pristine graphite and FGnPs were found to be 99.1 and 89.2 wt% at 1000 °C, respectively (Figure S2b, Supporting Information). The observed high thermal stability of the pristine graphite could be attributed to its structural integrity and large grain size (<150 μm). However, FGnPs displayed gradual weight loss up to 600 °C, attributable to the loss of absorbed moisture and oxygenated groups. In addition, a sharp weight loss (3.5 wt%) occurred over 600–700 °C with the maximum slope at 677 °C; a typical temperature for C–F bond dissociation.[21] This result is well accordance with the values obtained from XPS (3.0 at%) and EDS (3.4 at%) analyses (Table S1, Supporting Information). The high dissociation temperature implies the high stability of C–F bonds.

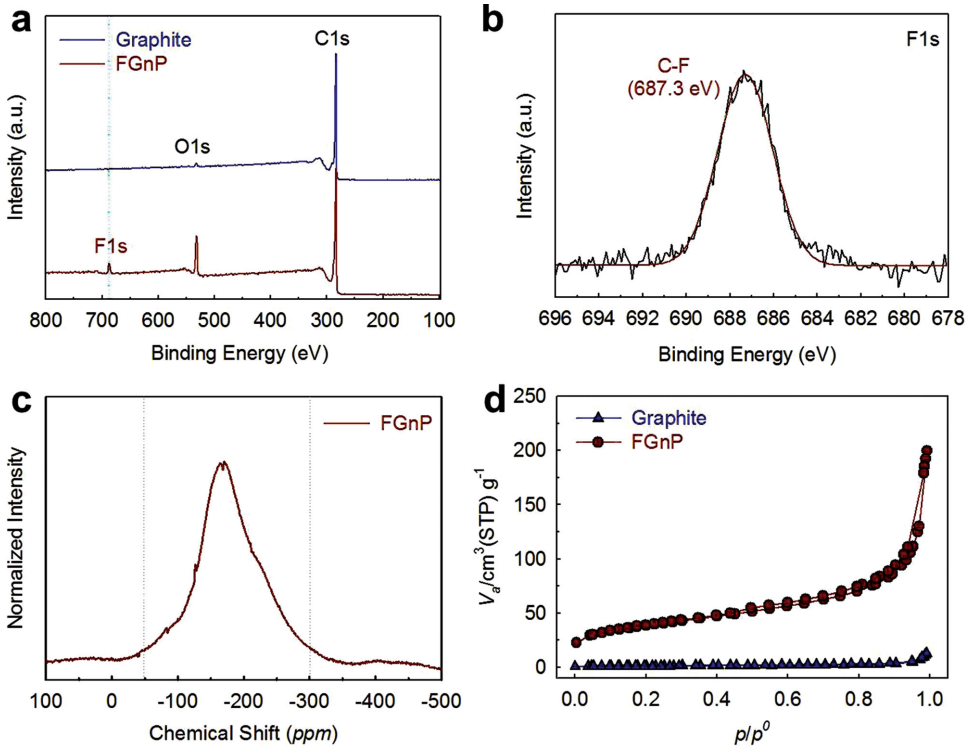

Figure 2. Characterization of the pristine graphite and FGnPs: a) XPS survey spectra of the pristine graphite and the as-prepared FGnPs, indicating that the occurrence of fluorination with a fluorine content of 3.0 at%; b) high-resolution F1s peak of FGnPs, showing the formation of graphitic C–F; c) ^{19}F MAS NMR spectrum of FGnPs, displaying characteristic peak attributed to sp^2 C–F bonds; the line broadening is due to strong ^{19}F–^{19}F homonuclear dipolar coupling of C–F bonds at the different edges, such as armchair C–F and zigzag C–F; d) nitrogen adsorption/desorption isotherms of the pristine graphite and FGnPs obtained at 77 K, exhibiting significant increase in specific surface area for FGnPs.

The degree of delamination caused by ball-milling could be estimated by comparing the intensity of [002] peak from X-ray diffraction (XRD). As seen in Figure S2c, Supporting Information, the pristine graphite shows a strong and sharp [002] peak at 26.5° corresponding to an interlayer *d*-spacing (0.34 nm) of graphitic layers,[22] whereas FGnPs show only about 0.27% intensity at 25.4° to the [002] peak of the graphite. These results implicated that the graphitic layers in the pristine graphite were exfoliated to a large extent into a few layers of FGnPs even in solid state, which should be a good precursor for further delamination upon dispersion in appropriate solvents. In addition to XRD patterns (Figure S2c, Supporting Information), the degree of delamination of FGnPs could also be roughly estimated from surface area measurements.[23] Specific surface area of FGnPs was thus compared with that of the pristine graphite using the Brunauer–Emmett–Teller (BET) measurement by nitrogen adsorption/desorption at 77 K (Figure 2d). The pristine graphite has low specific surface area of 2.78 $m^2\ g^{-1}$ (Table S2, Supporting Information), due to its highly ordered multilayered structure with strong π–π stacking. The specific surface area of FGnPs was increased 48.5 times to 134.79 $m^2\ g^{-1}$ (Table S2, Supporting Information) compared with that of the pristine graphite. Large surface area of FGnPs is expected to bring positive effects on electrochemical and device performance. The sorption isotherm of FGnPs is a type IV, which is typically associated with mesopores.[24] These results indicated that FGnPs were significantly exfoliated into a few graphitic layers ($2630/135 \approx 20$) by ball-milling and edge-fluorination. Although the observed specific surface area of FGnPs in the solid state was much smaller than that of the edge-carboxylated GnPs[12] and other edge-halogenated GnPs (XGnPs, X = Cl, Br, I),[25] the charge polarization at the edges of FGnPs must be stronger than that of other edge-functionalized GnPs due to the highest electronegativity of fluorine atoms. Hence, FGnPs are expected to be a good precursor for further delamination upon dispersion in polar solvents for enhanced processability.

Since FGnPs contain not only fluorine but also some oxygenated groups at their edges, they are dispersible well in polar solvents, such as water, ammonium hydroxide, methanol, ethanol, tetrahydrofuran (THF), acetone, *N*,*N*-dimethylformamide (DMF), *N*,*N*-dimethylacetamide (DMAc), and *N*-methyl-2-pyrrolidone (NMP), and even some of nonpolar solvents, including toluene and xylene (Figures S7a,b, Supporting Information). The stability of dispersion could be determined by zeta-potential measurements. Various concentrations of FGnPs dispersed in NMP show the zeta-potential values in the range of −33.5 to −48.7 mV (Figure S7c and Table S4, Supporting Information). The absolute value higher than ±30 mV implicates a stable dispersion.[26,27] Furthermore, the surface polarity of FGnPs was also determined by contact angle measurements. The average contact angle of a silicon wafer (as reference) and a FGnP film solution-cast from NMP solution onto a silicon wafer was 48.3° and 79.8°, respectively (Figure S7d, Supporting Information). Despite the coexistence of oxygenated functional groups, the presence of fluorine at the edges make FGnPs to be less hydrophilic to facilitate dispersion in nonpolar solvents, providing additional options for solution processing.

Raman spectroscopy was also utilized for the structural assessments of samples. As expected, the pristine graphite exhibits a sharp G band at 1585 cm^{-1} without detectable D band (Figure S2d, Supporting Information) due to highly ordered nature of the pristine graphite. As a result of the delamination and edge-fluorination of graphitic layers, however, the G band of FGnPs appeared at a higher frequency (centered at 1587 cm^{-1}) than the pristine graphite (1585 cm^{-1}) (Figure S2d, Supporting Information) due to the merging of G and G′ bands caused by the defects, transformation from graphite to a few layer graphene sheets, and resonation of isolated double bonds.[28] Furthermore, FGnPs show a strong and broad D band at 1359 cm^{-1} with a high I_D/I_G ratio of 0.92 due to the edge defects from the grain size reduction (<300 nm, see Figure 1c) and edge-fluorination.

In view of the well-defined structure and properties from the edge-fluorination, we further evaluated electrochemical performances of FGnPs for potential applications in DSSCs. For the use as counter electrodes (CEs) in DSSCs, thin films of FGnPs on fluorine-doped SnO_2 (FTO)/glass were prepared by using an electrostatic spray (e-spray) technique.[29] Edge-hydrogenated GnPs (HGnPs)[13] and Pt-coated FTO were also fabricated as the reference electrodes, and their fabrication details were described in the Supporting Information. Top and cross-sectional SEM images of the FTO glass plates with and without the HGnPs and FGnPs coatings are shown in Figure S8, Supporting Information. So far, there has only been one report on fluorine-functionalized graphene (F-graphene) as a CE in a DSSC based on an I^-/I_3^- redox couple.[30] Meanwhile, that the utilization of FGnPs as a CE for DSSCs in conjunction with a $Co(bpy)_3^{2+/3+}$ redox couple (bpy = 2′,2′-bipyridine) exhibited a higher open circuit voltage (V_{oc}) than the I^-/I_3^- redox couple has not been investigated. Electrocatalytic activities of the resultant electrodes were tested with symmetrical dummy cells by using two identical electrodes (Figure S9a, Supporting Information). Cyclic voltammetry (CV) was performed for all the symmetric dummy cells from −0.65 V to 0.65 V at a scan rate of 50 mV s^{-1} at room temperature, and the voltammogram characteristics are shown in Figure S9b, Supporting Information, which implies that HGnPs have poor interfacial charge-transfer activity toward the $Co(bpy)_3^{3+}$ ions since there are fewer active edges in its crystal lattice. The current–voltage response of a dummy cell should be simply the Ohmic-like straight line if the interfacial charge transfer and the mass transport in the electrolyte solution are sufficiently fast (Figure S9b, Supporting Information).[31] The inverse slope of the linear part near 0 V is the overall cell resistance (R_{CV}) related to the interface between an electrolyte and a CE, which also characterizes the electrocatalytic activity of the CE materials.[31] The R_{CV} for the FGnPs (7.1 Ω cm^2) was much lower than those of Pt–CE (11.5 Ω cm^2) and HGnP–CE (183.5 Ω cm^2), indicating a faster kinetics for reduction of $Co(bpy)_3^{3+}$ at the FGnP/electrolyte interface than other CE/electrolyte interfaces.

The current density is representative of the ionic carriers in the electrolytes solution between two electrodes of the symmetrical dummy cells. Here, the diffusion coefficient is proportional to J_{lim} as expressed in Equation (1)[32]

$$J_{lim} = 2nFC_{Co(bpy)_3^{3+}} D/\delta \quad (1)$$

where, δ is the inter-electrode distance, n is 1, the number of electron contributing to the charge transfer, F is Faraday's

constant, and C is concentration of transport limited species ($Co(bpy)_3^{3+}$) per unit volume, respectively. **Figure 3**a shows the Tafel-polarization curves of the symmetrical dummy cells configured with different electrodes. As clearly observed in the Tafel plots, the slopes of both cathodic and anodic parts are increased for FGnPs in comparison to those of Pt. This is because the more electronegative fluorine (χ = 3.98) than carbon (χ = 2.55) leads to the formation of polar covalent C–F bonds at the edges of FGnPs to impart higher electrochemical activities and better in-plane charge transfer properties than HGnPs. Due to the enhancement from edge-fluorination, the calculated diffusion coefficient of $Co(bpy)_3^{3+}$ for the FGnP electrode was 8.6×10^{-6} cm^2 s^{-1}, which is higher than that of the Pt electrode (5.8×10^{-6} cm^2 s^{-1}). Therefore, the result further supports the fact that the edges of graphene display more catalytic effects than the basal areas.[30,33,34] The mass transport can also be characterized by a potential-step chronoamperometry (CA, Figure S10, Supporting Information).

The CE in a liquid-junction DSSC serves for reduction of the oxidized state of redox mediators, which is created by the reaction with oxidized dye near the photoanode. The rate of the reduction at the CE should be comparable to the rate of dye regeneration at the photoanode, which can be expressed by the photocurrent density (J_{sc}). Hence, to avoid electron losses at the CE, the J_{sc} should be comparable to the exchange current density (J_0) at the CE, as shown in Equation (2)[35]

$$J_0 = RT/nFR_{ct} = Fk_0(C_{ox}^{1-\alpha} \cdot C_{red}^{\alpha}) \quad (2)$$

where R is the gas constant, T is the temperature, F is the Faraday's constant, and n is the number of electrons involved in the electrochemical reduction of redox couple at the CE. The k_0 is the rate constant of the electrode reaction at steady-state condition, C_{ox} and C_{red} are the concentrations of oxidized and reduced mediators, respectively, and α is 0.5 as the charge-transfer coefficient in symmetrical electrode kinetics. The J_0 is a kinetic component that arises due to the charge transfer from the CE to the oxidized mediator ions at the CE/electrolyte interface. Therefore, the cathodic electrocatalytic activity is assessed by R_{ct}, J_0, and/or k_0. To gain more insights into the electrocatalytic activity of the sample electrodes, electrochemical impedance spectroscopic (EIS) measurements were made on the symmetrical dummy cells. Figure 3b shows the Nyquist plots of the EIS spectra and the corresponding equivalent circuit (EC) model[31] for fitting the EIS spectra (inset, Figure 3b). In this model, the R_{ct} is directly related to a reaction barrier in the reduction of the redox couple at the CE surface, and hence it should be considered as an important parameter to evaluate the electrocatalytic activities of the catalysts. The double-layer capacitance (C_{dl}), the corresponding capacitance from constant phase element (CPE), stems from the charge accumulation at the CE/electrolyte interface and depends on the effective surface area of the interface.[31] The Nernst diffusion impedance (Z_W) describes the diffusion of the redox couple between two electrodes. As shown in Figure 3b, EIS spectra exhibited two distinct semicircles offset from the origin in the Nyquist plots, which correspond to the charge transfer impedance (R_{ct} and C_{dl})

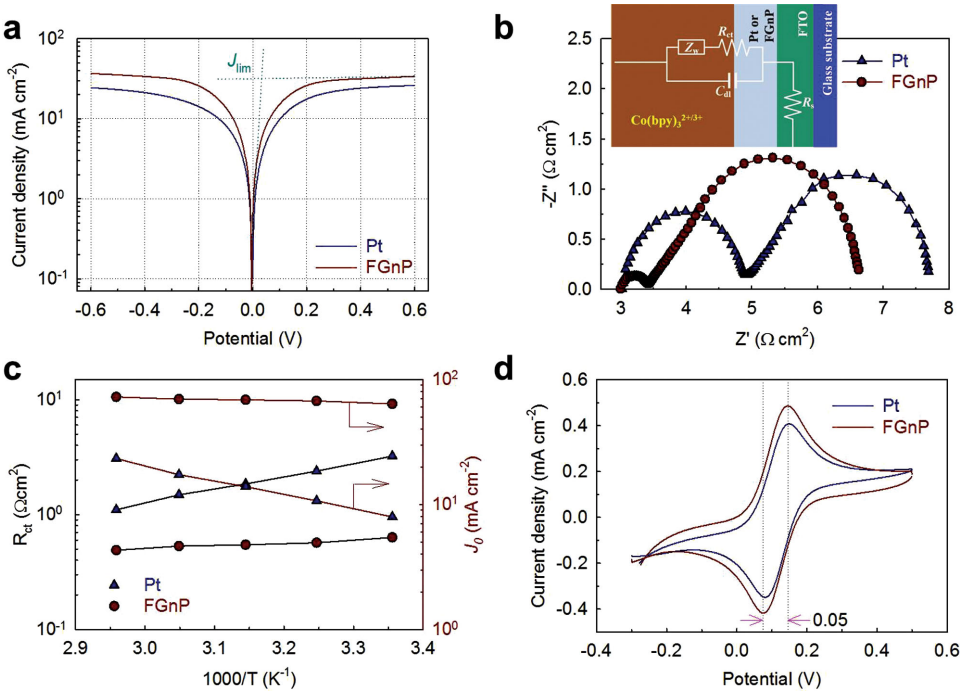

Figure 3. DSSC performance of the platinum (Pt) and FGnP electrodes: a) Tafel-polarization curves; b) Nyquist plots of the Pt and FGnP dummy cells with $Co(bpy)_3^{2+/3+}$ in acetonitrile measured at 0 V from 10^6 to 0.1 Hz. The inset is the equivalent circuit for fitting the EIS spectra; c) Arrhenius plot of R_{ct} and J_0 versus temperature; d) cyclic voltammograms (CV) obtained at a scan rate of 50 mV s^{-1} for oxidation/reduction of the $Co(bpy)_3^{2+/3+}$ redox couple using Pt and FGnP electrodes as the working electrodes, a Pt wire as the CE, Ag/Ag^+ as the reference electrode, and 0.1 M $LiClO_4$ as the supporting electrolyte.

and diffusion impedance (Z_W), respectively. The estimated EIS values were listed in Table S5, Supporting Information. The R_{ct} of the HGnP electrode (121.03 Ω cm^2, Figure S9c, Supporting Information) was significantly reduced by edge-fluorine doping in FGnPs (0.29 Ω cm^2), whose value is much lower than that of the conventional Pt electrode (0.93 Ω cm^2). These results are well accordance with the aforementioned values obtained from the CV measurements. Furthermore, the temperature dependences of the R_{ct} of Pt and FGnPs are shown as Nyquist plots in Figure S11, Supporting Information. These results indicate that the J_0 of the Pt and FGnP electrodes show a temperature dependence (Figure 3c, right ordinate), following the Arrhenius Equation (3)[36]

$$J_0 = I_0 e^{-(E_a/RT)} \quad (3)$$

where E_a is the activation energy and I_0 is the exchange current density at T = infinite. The results illustrate that the R_{ct} decreases as exchange-current density increases with increasing temperature. Likewise, decreases in charge-transfer resistance are also associated with the increase in the exchange-current density J_0 calculated using Equation (3) at the CE/electrolyte interface. As explained earlier, the creation of active sites by charge polarization at the edges of FGnPs contributes to enhancement of the catalytic activity of the graphene layers for $Co(bpy)_3^{3+}$ reduction.

Figure 3d shows the cyclic voltammograms of the $Co(bpy)_3^{2+/3+}$ redox couple on Pt and FGnP electrodes, respectively. A typical pair of oxidation and reduction peaks revealed in the voltage range of –0.3 to 0.5 V (vs Ag/Ag$^+$). The peak-to-peak separation (E_{pp}) for a pair peak and the peak currents are two important parameters for comparing catalytic activities of different CEs. A smaller E_{pp} and larger peak currents indicate higher catalytic performance. The E_{pp} is almost the same between Pt and FGnP electrodes, whereas the cathodic peak currents for the reduction of $Co(bpy)_3^{3+}$ are 0.41 and 0.49 mA cm^{-2} for Pt and FGnP electrodes, respectively. This indicates that the reduction rate of $Co(bpy)_3^{3+}$ to $Co(bpy)_3^{2+}$ on the FGnP electrode surface is faster than that on the Pt counterpart. Furthermore, oxygens in FGnPs are also relatively high charge polarization, which might also be good affinity with the positively charged Co-complex redox couple.[37]

For evaluation of electrochemical stability of the sample electrodes, freshly assembled symmetrical dummy cells were first measured with CV at room temperature. Then, they were subjected to EIS (Figure S12, Supporting Information) and followed by CV measurements again. Despite cycling potentials, the semicircles in the low-frequency range exhibited a similar shape in the Nyquist plots of the Pt and FGnP electrodes (Figure S12, Supporting Information). These similar curves between the two electrodes indicate that the $Co(bpy)_3^{2+/3+}$ redox couple is invariant with the surface conditions at the electrodes. However, the R_{ct} of the Pt electrode significantly increased compared to that of the FGnP electrode as the cycling potential was repeated. Figure S12c, Supporting Information, shows the electrochemical stability of symmetrical dummy cells with Pt and FGnP electrodes as function of R_{ct} versus EIS scanning number under cumulative potential-cycling with $Co(bpy)_3^{2+/3+}$ in acetonitrile. The R_{ct} for the Pt electrode was 6.72 Ω cm^2 in the first cycle (e.g., after 100 CV cycles), but it was remarkably increased up to 50.38 Ω cm^2 in the final cycle (e.g., after 1000 CV cycles). On the other hand, the FGnP electrode exhibited a R_{ct} of 0.83 and 1.08 Ω cm^2 in the first and final cycles, respectively. Electrocatalytic performance of the FGnP electrode was maintained by ≈80% after 1000 cycling potentials, whereas the R_{ct} of Pt electrode decreased below 20% in the final cycle. On basis of the above results, we can conclude that the FGnP electrode had better electrocatalytic activity and electrochemical stability than those of the Pt electrode in $Co(bpy)_3^{3+/2+}$ medium.

The catalytic activity of the sample electrodes as CEs in actual DSSCs was evaluated in a $Co(bpy)_3^{2+/3+}$ redox couple with an organic sensitizer (JK-306)[38] and a multifunctional coadsorbent of HC-A (SGT-301, see the Supporting Information).[39,40] **Figure 4**a shows the current–voltage (J–V) curves and their photovoltaic parameters were summarized in Table S6, Supporting Information. The DSSC based on the FGnP–CE displayed a higher photovoltaic performance (FF, J_{sc}, and PCE: 71.5%, 14.44 mA cm^{-2}, and 10.01%, respectively) than that with the Pt–CE (69.8%, 14.28 mA cm^{-2}, and 9.61%) and HGnP–CE

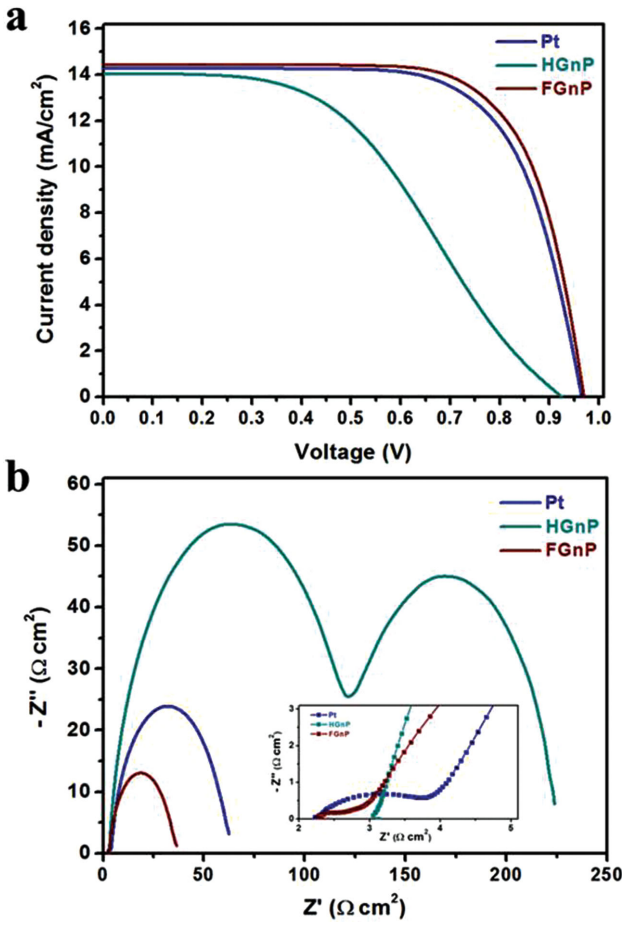

Figure 4. a) Current–voltage curves of the DSSCs with the Pt, HGnP, and FGnP CEs on $Co(bpy)_3^{2+/3+}$ redox couple under one sun illumination (AM 1.5 G). The TiO_2 film thickness and active area are 8 (5 + 3) μm and 0.16 cm^2 with a black metal mask, respectively. (b) Nyquist plots in full-frequency region of DSSCs with different CEs at an applied bias of –0.92 V under dark conditions. The inset shows Nyquist plots in high-frequency region of same DSSCs.

(45.8%, 14.05 mA cm^{-2}, and 5.96%). Moreover, the different performance of the DSSCs with different CEs was confirmed by EIS measurements under dark conditions (Figure 4b). The R_s and R_{ct} at the CEs/electrolyte interface calculated with an EC (Figure S13, Supporting Information) of the DSSC with a FGnP–CE are 2.24 and 0.47 Ω cm^2, respectively, whereas the corresponding values of the DSSCs are 2.27 and 1.87 Ω cm^2 for the Pt–CE and 3.1 and 122.9 Ω cm^2 for the HGnP–CE. The lower R_{ct} value for the FGnPs suggests high electrocatalytic activity for the reduction of $Co(bpy)_3^{3+}$ ions, which could enhance the DSSC performance, in particular, FF and J_{sc} (Table S6, Supporting Information).

Apart from the DSSC study described above, we further found that FGnPs are also ideal electrode materials for LIBs. Over the past decades, to enhance the electrochemical performance and the operating safety of lithium ion batteries, many efforts have been devoted to develop fluorinated electrode materials (especially, fluorinated cathode materials), as well as fluorinated salts for electrolytes and fluorinated binders.[41] Hence, we also investigated FGnPs as an anode material for energy storage in LIBs.

The initial discharge/charge profiles of HGnPs and FGnPs at 0.1 C in the voltage range of 0.02–3 V are shown in **Figure 5**a, which are in accordance with the CV analysis. Figure S14, Supporting Information, shows the initial five cycles of CV profiles for HGnPs and FGnPs at a scan rate of 0.1 mV s^{-1} in the voltage range of 0.02–3 V. The first cathodic peak (C_a) centered at around 0.6 V in the 1st cycle and then disappeared in the following cycles indicates a dense solid electrolyte interphase (SEI) layer formation on the surfaces of HGnPs and FGnPs in the first cycle. The second cathodic peak (C_b) centered at 0.05 V is ascribed to lithium ions insertion into HGnPs and FGnPs.[42] Such electrochemical behavior is typical for carbonaceous materials as anodes in LIBs.[43] To compare the rate capability

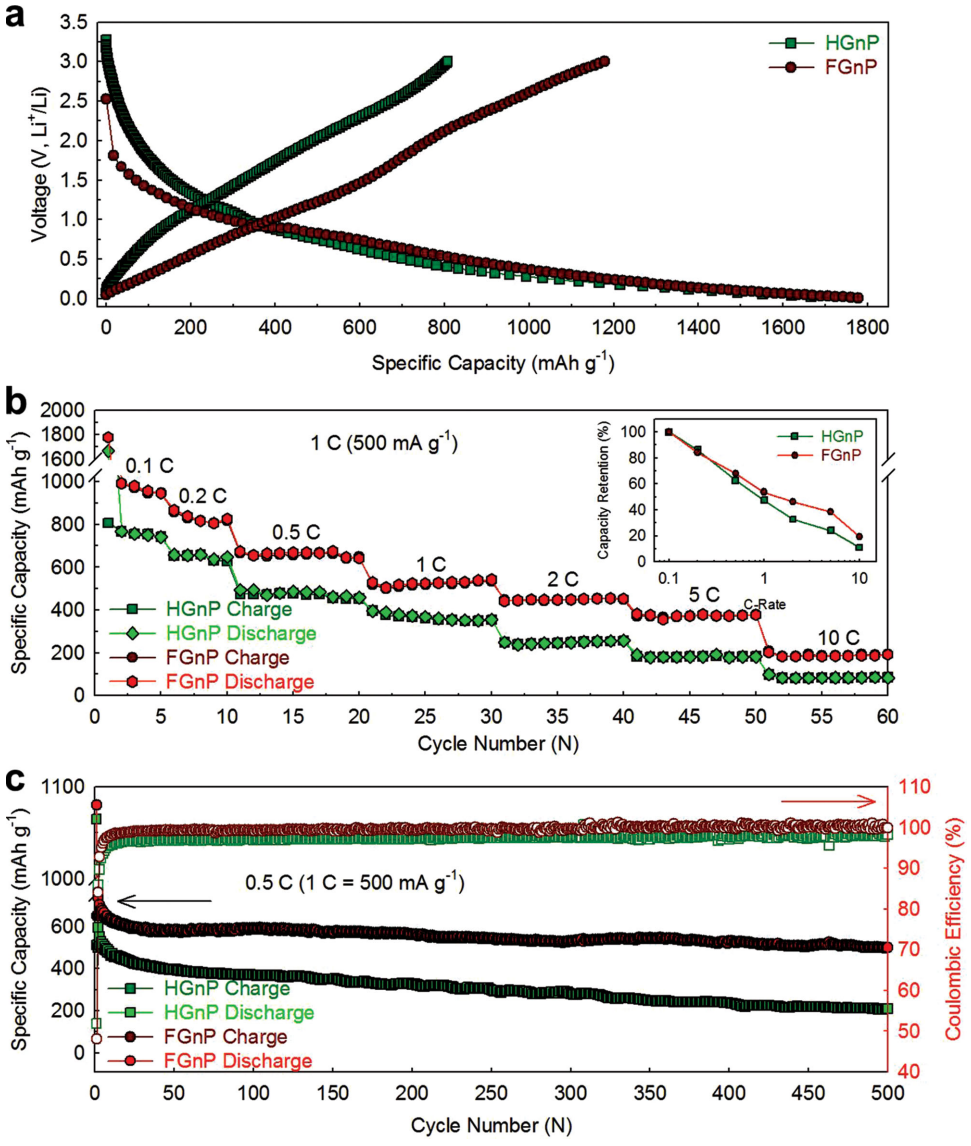

Figure 5. LIB performance of HGnP and FGnP anodes: a) Initial discharge/charge curves at 0.1 C; b) rate performance (Inset: Charge capacity retention at various current densities); c) cycling performance and coulombic efficiency at 0.5 C of HGnPs and FGnPs in the voltage range of 0.02–3 V.

of HGnPs and FGnPs, the cells were tested for 60 cycles at current densities varying from 0.1 to 10 C in the voltage ranges of 0.02–3 V. As shown in Figure 5a,b, the FGnPs and HGnPs delivered the initial discharge capacities of 1778.1 (FGnPs) and 1666.9 mAh g^{-1} (HGnPs) at 0.1 C with charge capacities of 1176.3 (FGnPs) and 807.4 mAh g^{-1} (HGnPs), respectively, indicating the higher initial coulombic efficiency of 66.2% for FGnPs than 48.4% for HGnPs. Furthermore, as shown in the inset of Figure 5b, FGnPs also showed the higher rate capability than HGnP at >0.5 C.

In Figure 5c, the relatively long-term cycling performance and the coulombic efficiency for HGnPs and FGnPs are compared at 0.5 C in the voltage range of 0.02–3 V. FGnPs electrode could deliver an initial charge capacity of 650.3 mAh g^{-1} at 0.5 C in the voltage of 0.02–3 V, which are higher than that of the conventional graphite-based electrode (a theoretical capacity of 373 mA g^{-1})[44] and the reference HGnPs with 511.3 mAh g^{-1} (Figure 5c). Even, after 500 cycles, FGnP can still maintain higher capacity of 498.2 mAh g^{-1} with a capacity retention of 76.6% than HGnPs (208.5 mAh g^{-1}, 40.8%), further indicating better cycling performance for FGnPs than that of HGnPs. Compared with ≈100% coulombic efficiency in the following cycles (Figure 5c), it should be noted that the lower initial coulombic efficiency not only for HGnPs but also for FGnPs (Figure 5a,c) is most likely resulted from the interaction between lithium ions and the residual oxygenated functional groups within HGnPs and FGnPs, such as carboxylic acid, hydroxyl groups, and oxyfluorides.[45] The rich residual oxygen functional groups of electrode material could decrease the initial coulombic efficiency of cell. However, the cycling stability of the cell can be significantly improved over the cycles due to a dense SEI formation in the initial cycle. The formation of a dense SEI is related to the surface defects, the strength bond of C–F at the edges (488 kJ mol^{-1}) and oxygen containing functional groups of the electrode materials and it, once formed, can serve as important factors to affect the electrochemical process, such as electronic/ionic conductivity. As shown in Figure S14, Supporting Information, the higher intensity ratio of (I_{Ca}/I_{Cb}) in the first cycle supports that FGnPs form a denser SEI film than HGnPs. Apart from the strong SEI formation, the excellent rate capability and cycling performance of FGnPs are also attributed to the higher electronegativity of fluorine (χ = 3.98) at the edges of FGnPs creating net positive charge on adjacent carbon atoms (χ = 2.55) to facilitate lithium extraction from/insertion into the electrode during cycling.

Electrochemical impedance spectroscopy[46] was widely used to investigate the kinetics of the electrode materials for LIBs. Figures S15a,b, Supporting Information, show the Nyquist plots of the HGnP and FGnP electrodes at the discharged state of 1.0 V (vs Li^+/Li) at different temperatures after discharge/charge for five cycles. All the impedance curves of HGnPs and FGnPs show a semicircle in the medium frequency region, which could be assigned to the lithium ion diffusion through the SEI film (R_s) and the charge transfer resistance (R_{ct}), respectively. A clear ≈45° inclined line in the low-frequency range could be considered to be a Warburg impedance (W). The R_{ct} is calculated using the equivalent circuit as shown in Figure S16, Supporting Information, which also includes electrolyte resistance (R_e), a constant phase element (CPE-1), and a nonideal constant phase element (CPE-2). The values of R_e, R_s, and R_{ct} obtained from a nonlinear least squares fitting are summarized in Figure S18 and Table S7, Supporting Information. As can be seen, FGnPs showed smaller R_e, R_s, and R_{ct} values than those of HGnPs at different temperatures, indicating, once again, the higher electrolyte/electrode saturation, easier SEI formation, and enhanced kinetics for FGnPs than those of HGnPs. The kinetics of the charge-transfer reaction for HGnPs and FGnPs was further investigated by the apparent activation energy.[47] The exchange current (i_0) and the apparent activation energy (E_a) for HGnPs and FGnPs electrodes can be calculated from the Arrhenius equation: i.e., Equations (4) and (5), respectively

$$i_0 = RT/(nFR_{ct}) \tag{4}$$

$$i_0 = A\ \exp(-E_a/RT) \tag{5}$$

where A is a temperature-independent coefficient, R is the gas constant, T (K) is the absolute temperature, n is the number of transferred electrons, F is the Faraday constant, and E_a is apparent activation energy. Figure S15c, Supporting Information, shows Arrhenius plots of $\log_{10} i_0$ as a function of $1/T$. The apparent activation energies ($E_a = -Rk\ln 10$, where k = the slope of the fitting line in Figure S15c, Supporting Information) of HGnPs and FGnPs were calculated to be 38.7 and 35.5 kJ mol^{-1}, respectively. Compared to HGnPs, FGnPs with lower apparent activation energy indicate the easier extraction/insertion of lithium ions from the stable host structures and thus further support its better electrochemical performance than that of HGnPs, as shown in Figure 5 and Figure S17, Supporting Information.

3. Conclusion

In summary, we have, for the first time, prepared edge-fluorinated graphene nanoplatelets by using simple but efficient mechanochemical ball-milling method, which is considered to be a new general approach for mass production of edge-functionalized GnPs at low cost. The fluorination at the edges of GnPs was confirmed by using various analytical techniques, including EA, XPS, Raman, XRD, TGA, EDS, BET, SEM, STEM, and ^{19}F-NMR. The resultant FGnPs show a good dispersibility, allowing for device fabrications using all-solution processing. Due to the highest electronegativity of fluorine atom (χ = 3.98) and the strongest single covalent bond (C–F, 488 kJ mol^{-1}) at the edges, FGnPs were demonstrated to show the significantly enhanced electrochemical performance in DSSCs and LIBs with excellent cycling stability. These results indicate that FGnPs can be a killer material to solve current issues related to conventional electrode materials for energy conversion and storage.

4. Experimental Section

Materials: Graphite was obtained from Alfa Aesar (Natural, −100 mesh, 99.9995% metals basis, #14735) and used as received. F_2/Ar (20 vol%) gas was purchased from RIGAS, Inc. (Daejeon Metropolitan City, Korea) and used as received. All other solvents were

supplied by Aldrich Chemical, Inc., and used without further purification, unless otherwise specified.

Syntheses of FGnPs: FGnPs were prepared by a simple ball-milling graphite in a planetary ball-mill capsule. Graphite (5.0 g) was placed into a stainless steel capsule containing stainless steel balls (500 g, diameter 5 mm). After five cycles of charging argon gas (10 bar) and discharging under reduced pressure (0.05 mmHg), the capsule was then fixed in the planetary ball-mill machine and agitated with 500 rpm for 48 h. Argon gas was removed and diluted fluorine (20 vol% in Ar) gas was slowly charged (5 bar). After standing for 24 h, the resultant product was Soxhlet extracted with 1 M aq. HCl solution to get rid of remaining metallic impurities, if any. Final product was then freeze-dried at −120 °C under a reduced pressure (0.05 mmHg) for 48 h to yield 5.15 g of dark black FGnP powder (contained at least 0.15 g of fluorine: ≈3.0 wt%).

Instrumentation: Elemental analysis (EA) was conducted with Thermo Scientific Flash 2000. The FE-SEM was performed on FEI Nanonova 230. STEM images were acquired on a probe-corrected JEOL ARM200F operated at 200 kV equipped with a cold field emission gun, a high resolution pole-piece, and a Centurio EDS detector with a collection solid angle of ≈1 Sr. Images and EDS maps were acquired at a probe current of 90 pA. The elemental mapping was carried out by EDS using the JSM-7500FA. The surface area was measured by nitrogen adsorption–desorption isotherms using the BET method on Micromeritics ASAP 2504N. XPS were recorded on a Thermo Fisher K-alpha XPS spectrometer. TGA was conducted on a TA Q200 (TA Instrument) under nitrogen at a heating rate of 10 °C min^{-1}. Micro-Raman measurements were made with a WiTec Alpha300S system with 532 nm wavelength laser light and a 50× objective. XRD patterns were recorded on a Rigaku D/MAZX 2500V/PC with Cu–Kα radiation (35 kV, 20 mA, $\lambda = 1.5418$ Å). Zeta-potential values were determined using Malvern Zetasizer (Nano ZS, Malvern Instruments). Solid-state ^{19}F MAS NMR spectroscopic measurements were performed on a Varian Unitylnova 600 (600 MHz) spectrometer. Contact angle measurements were conducted on a Krüss DSA 100 contact angle analyzer. Sample solutions were coated on a silicon (Si) wafer, dried, and measured using water drop.

Supporting Information

Supporting Information is available from the Wiley Online Library or from the author.

Acknowledgements

This research was supported by CRI (2014069102), MCR, BK21 Plus, BRL, MSIP programs through the National Research Foundation (NRF) of Korea, ICET through KETEP, AFOSR-AOARD, the Australia AutoCRC 2020, Australia LE120100104, and AFOSR (FA9550-12-1-0037, FA-9550-12-1-0069). I.Y.J., M.J.J., and J.X. contributed equally to this work.

Received: October 31, 2014
Revised: November 28, 2014
Published online: January 8, 2015

[1] T. B. Johansson, L. Burnham, *Renewable Energy: Sources for Fuels and Electricity*, Island Press, Washington DC **1993**.
[2] A. S. Aricò, P. Bruce, B. Scrosati, J.-M. Tarascon, W. van Schalkwijk, *Nat. Mater.* **2005**, *4*, 366.
[3] A. K. Geim, K. S. Novoselov, *Nat. Mater.* **2007**, *6*, 183.
[4] T. O. Wehling, K. S. Novoselov, S. V. Morozov, E. E. Vdovin, M. I. Katsnelson, A. K. Geim, A. I. Lichtenstein, *Nano Lett.* **2008**, *8*, 173.
[5] M. D. Stoller, S. Park, Y. Zhu, J. An, R. S. Ruoff, *Nano Lett.* **2008**, *8*, 3498.
[6] A. Fasolino, J. H. Los, M. I. Katsnelson, *Nat. Mater.* **2007**, *6*, 858.
[7] A. A. Balandin, S. Ghosh, W. Bao, I. Calizo, D. Teweldebrhan, F. Miao, C. N. Lau, *Nano Lett.* **2008**, *8*, 902.
[8] L. J. Hardwick, M. Marcinek, L. Beer, J. B. Kerr, R. Kostecki, *J. Electrochem. Soc.* **2008**, *155*, A442.
[9] V. A. Sethuraman, L. J. Hardwick, V. Srinivasan, R. Kostecki, *J. Power Sources* **2010**, *195*, 3655.
[10] Y.-G. Guo, J.-S. Hu, L.-J. Wan, *Adv. Mater.* **2008**, *20*, 2878.
[11] J. T. Robinson, J. S. Burgess, C. E. Junkermeier, S. C. Badescu, T. L. Reinecke, F. K. Perkins, M. K. Zalalutdniov, J. W. Baldwin, J. C. Culbertson, P. E. Sheehan, E. S. Snow, *Nano Lett.* **2010**, *10*, 3001.
[12] I.-Y. Jeon, Y.-R. Shin, G.-J. Sohn, H.-J. Choi, S.-Y. Bae, J. Mahmood, S.-M. Jung, J.-M. Seo, M.-J. Kim, D. W. Chang, L. Dai, J.-B. Baek, *Proc. Natl. Acad. Sci. U.S.A.* **2012**, *109*, 5588.
[13] I.-Y. Jeon, H.-J. Choi, S.-M. Jung, J.-M. Seo, M.-J. Kim, L. Dai, J.-B. Baek, *J. Am. Chem. Soc.* **2013**, *135*, 1386.
[14] I.-Y. Jeon, S. Zhang, L. Zhang, H.-J. Choi, J.-M. Seo, Z. Xia, L. Dai, J.-B. Baek, *Adv. Mater.* **2013**, *25*, 6138.
[15] A. Allouche, Y. Ferro, *Carbon* **2006**, *44*, 3320.
[16] A. Mathkar, T. N. Narayanan, L. B. Alemany, P. Cox, N. Patrick, G. Gao, P. Chang, R. Romero-Aburto, S. A. Mani, P. M. Ajayan, *Part. Part. Syst. Charact.* **2013**, *30*, 266.
[17] Y. Ahmad, M. Dubois, K. Guérin, A. Hamwi, Z. Fawal, A. P. Kharitonov, A. V. Generalov, A. Y. Klyushin, K. A. Simonov, N. A. Vinogradov, I. A. Zhdanov, A. B. Preobrajenski, A. S. Vinogradov, *J. Phys. Chem. C* **2013**, *117*, 13564.
[18] J. Giraudet, M. Dubois, K. Guérin, J. P. Pinheiro, A. Hamwi, W. E. E. Stone, P. Pirotte, F. Masin, *J. Solid State Chem.* **2005**, *178*, 1262.
[19] I. P. Asanov, L. G. Bulusheva, M. Dubois, N. F. Yudanov, A. V. Alexeev, T. L. Makarova, A. V. Okotrub, *Carbon* **2013**, *59*, 518.
[20] V. P. Fadeeva, V. D. Tikhova, O. N. Nikulicheva, *J. Anal. Chem.* **2008**, *63*, 1094.
[21] J.-B. Baek, F. W. Harris, *Macromolecules* **2005**, *38*, 1131.
[22] Z. Q. Li, C. J. Lu, Z. P. Xia, Y. Zhou, Z. Luo, *Carbon* **2007**, *45*, 1686.
[23] M.-J. Kim, I.-Y. Jean, J.-M. Seo, L. Dai, J.-B. Baek, *ACS Nano* **2014**, *8*, 2820.
[24] J. Rouquerol, D. Avnir, C. W. Fairbridge, D. H. Everett, J. H. Haynes, N. Pernicone, J. D. F. Ramsay, K. S. W. Sing, K. K. Unger, *Pure Appl. Chem.* **1994**, *66*, 1739.
[25] I.-Y. Jeon, H.-J. Choi, M. Choi, J.-M. Seo, S.-M. Jung, M.-J. Kim, S. Zhang, L. Zhang, Z. Xia, L. Dai, N. Park, J.-B. Baek, *Sci. Rep.* **2013**, *3*, 1810.
[26] D. Hanaor, M. Michelazzi, C. Leonelli, C. C. Sorrell, *J. Eur. Ceram. Soc.* **2012**, *32*, 235.
[27] D. H. Everett, *Basic Principles of Colloid Science*, The Royal Society of Chemistry, London **1988**, p. 76.
[28] K. N. Kudin, B. Ozbas, H. C. Schniepp, R. K. Prud'homme, I. A. Aksay, R. Car, *Nano Lett.* **2008**, *8*, 36.
[29] M. J. Ju, J. C. Kim, H.-J. Choi, I. T. Choi, S. G. Kim, K. Lim, J. Ko, J.-J. Lee, I.-Y. Jeon, J.-B. Baek, H. K. Kim, *ACS Nano* **2013**, *7*, 5243.
[30] S. Das, P. Sudhagar, V. Verma, D. Song, E. Ito, S. Y. Lee, Y. S. Kang, W. Choi, *Adv. Funct. Mater.* **2011**, *21*, 3729.
[31] M. Liberatore, A. Petrocco, F. Caprioli, C. La Mesa, F. Decker, C. A. Bignozzi, *Electrochim. Acta* **2010**, *55*, 4025.
[32] A. Hauch, A. Georg, *Electrochim. Acta* **2001**, *46*, 3457.
[33] F. Schedin, *Nat. Nanotechnol.* **2010**, *5*, 487.
[34] J. D. Roy-Mayhew, D. J. Bozym, C. Punckt, I. A. Aksay, *ACS Nano* **2010**, *4*, 6203.
[35] S. Ahmad, E. Guillén, L. Kavan, M. Grätzel, M. K. Nazeeruddin, *Energy Environ. Sci.* **2013**, *6*, 3439.

[36] M. Wang, A. M. Anghel, B. Marsan, N.-L. C. Ha, N. Pootrakulchote, S. M. Zakeeruddin, M. Grätzel, *J. Am. Chem. Soc.* **2009**, *131*, 15976.
[37] M. J. Ju, I.-Y. Jeon, K. Lim, J. C. Kim, H.-J. Choi, I. T. Choi, Y. K. Eom, Y. J. Kwon, J. Ko, J.-J. Lee, J.-B. Baek, H. K. Kim, *Energy Environ. Sci.* **2014**, *6*, 3356.
[38] K. Lim, M. J. Ju, J. Na, H. Choi, M. Y. Song, B. Kim, K. Song, J.-S. Yu, E. Kim, J. Ko, *Chem. Eur. J.* **2013**, *19*, 9442.
[39] B. J. Song, H. M. Song, I. T. Choi, S. K. Kim, K. D. Seo, M. S. Kang, M. J. Lee, D. W. Cho, M. J. Ju, H. K. Kim, *Chem. Eur. J.* **2011**, *17*, 11115.
[40] I. T. Choi, M. J. Ju, S. H. Kang, M. S. Kang, B. S. You, J. Y. Hong, Y. K. Eom, S. H. Song, H. K. Kim, *J. Mater. Chem. A* **2013**, *1*, 9114.
[41] G. G. Amatucci, N. Pereira, *J. Fluorine Chem.* **2007**, *128*, 243.
[42] C. Wang, D. Li, C. O. Too, G. G. Wallace, *Chem. Mater.* **2009**, *21*, 2604.
[43] E. Yoo, J. Kim, E. Hosono, H.-S. Zhou, T. Kudo, I. Honma, *Nano Lett.* **2008**, *8*, 2277.
[44] D. Aurbach, B. Markovsky, I. Weissman, E. Levi, Y. Ein-Eli, *Electrochim. Acta* **1999**, *45*, 67.
[45] Z.-S. Wu, W. Ren, L. Xu, F. Li, H.-M. Cheng, *ACS Nano* **2011**, *5*, 5463.
[46] J. Vetter, P. Novák, M. R. Wagner, C. Veit, K. C. Möller, J. O. Besenhard, M. Winter, M. Wohlfahrt-Mehrens, C. Vogler, A. Hammouche, *J. Power Sources* **2005**, *147*, 269.
[47] Y. Yamada, Y. Iriyama, T. Abe, Z. Ogumi, *J. Electrochem. Soc.* **2010**, *157*, A26.